Supporting Information: A unified description of the optical phonon modes in N-layer $MoTe_2$

Guillaume Froehlicher,[1] Etienne Lorchat,[1] François Fernique,[1] Chaitanya Joshi,[2,3] Alejandro Molina-Sánchez,[2] Ludger Wirtz,[2] and Stéphane Berciaud[1,*]

[1] *Institut de Physique et Chimie des Matériaux de Strasbourg and NIE, UMR 7504, Université de Strasbourg and CNRS, 23 rue du Læss, BP43, 67034 Strasbourg Cedex 2, France*

[2] *Physics and Material Sciences Research Unit, University of Luxembourg, L-1511 Luxembourg, Luxembourg*

[3] *Department of Physics, Indian Institute of Technology Bombay, Powai, Mumbai-400076, India*

* stephane.berciaud@ipcms.unistra.fr

This document contains the following sections:

- Force constant model (Section SI)
- Bulk phonon frequencies (Section SII)
- Normal mode displacements (Section SIII)
- The empirical bond polarizability model (Section SIV)
- Raman Spectra from the bond polarizability model (Section SV)
- Ab-initio bulk phonon modes (Section SVI)
- Additional Raman measurements (Section SVII)

SI. FORCE CONSTANT MODEL

As explained in the main text, N-layer $MoTe_2$ is modeled as a one-dimensional finite linear chain composed of $2N$ Te atoms of mass per unit area μ_X and N Mo atoms of mass per unit area μ_M (see Fig. S1) [1]. Within one $MoTe_2$ layer, nearest neighbor Mo and Te atoms and the pair of second nearest neighbor Te atoms are connected by springs with force constants per unit area α and δ respectively. Interlayer interactions are described by two force constants per unit area β and γ between nearest neighbor Te atoms belonging to adjacent layers and between second nearest neighbor Mo and Te atoms, respectively. To account for surface effects, we consider effective force constants α_e and δ_e for the first and N^{th} layer. Since substrate effects have been shown to have a negligible influence on the Raman modes of MX_2[1–5], we assume that the two extreme layers are only connected to one layer, *i.e.,* we do not include an additional spring constant that would account for coupling of one of the outer layers to a substrate.

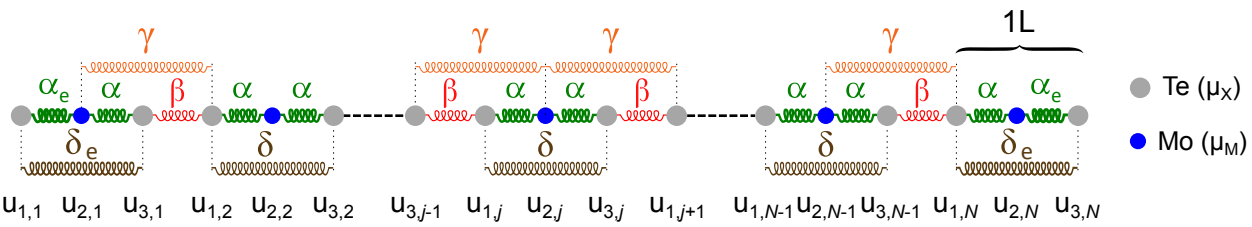

FIG. S1: Schematic of the finite linear chain model. μ_M (μ_X) is the mass per unit area of the Mo (Te) atom. α and β are the (intra-plane) force constants that connect the first nearest neighbor atoms. γ and δ are the (inter-plane) force constants that connect the second nearest neighbor atoms. $u_{i,j}$ is the displacement, with respect to the equilibrium position, of the i^{th} atom ($i = 1, 3$ for Te and $i = 2$ for Mo) in the j^{th} $MoTe_2$ layer ($j \in [\![1, N]\!]$).

We note $u_{i,j}$ the displacement, with respect to the equilibrium position, of the i^{th} atom ($i = 1, 3$ for Te and $i = 2$ for Mo) in the j^{th} $MoTe_2$ layer ($j \in [\![1, N]\!]$). We can then write the equations of motion using Newton's law. These equations form a system of $3N$ coupled differential equations that can be written as

$$\frac{\mathrm{d}^2\mathcal{U}}{\mathrm{d}t^2} = -\mathcal{D}\,\mathcal{U}, \tag{S1}$$

with the displacement vector $\mathcal{U} = \left(u_{1,1},\ u_{2,1},\ u_{3,1},\ \ldots,\ u_{i,j},\ \ldots,\ u_{1,N},\ u_{2,N},\ u_{3,N}\right)$ and the $3N \times 3N$ dynamical matrix

$$\mathcal{D} = \begin{pmatrix}
\frac{\alpha_e+\delta e}{\mu_X} & -\frac{\alpha_e}{\mu_X} & -\frac{\delta_e}{\mu_X} & \cdots & 0 & 0 & 0 & 0 & 0 & \cdots & 0 & 0 & 0 \\
-\frac{\alpha_e}{\mu_M} & \frac{\alpha_e+\alpha+\gamma}{\mu_M} & -\frac{\alpha}{\mu_M} & \ddots & \vdots & \vdots & \vdots & \vdots & \vdots & \ddots & \vdots & \vdots & \vdots \\
-\frac{\delta_e}{\mu_X} & -\frac{\alpha}{\mu_X} & \frac{\alpha+\beta+\gamma+\delta_e}{\mu_X} & \ddots & \vdots & \vdots & \vdots & \vdots & \vdots & \ddots & \vdots & \vdots & \vdots \\
0 & -\frac{\gamma}{\mu_X} & -\frac{\beta}{\mu_X} & \ddots & \vdots & \vdots & \vdots & \vdots & \vdots & \ddots & \vdots & \vdots & \vdots \\
\vdots & 0 & -\frac{\gamma}{\mu_M} & \ddots & \vdots & \vdots & \vdots & \vdots & \vdots & \ddots & \vdots & \vdots & \vdots \\
\vdots & \vdots & 0 & \ddots & \vdots & \vdots & \vdots & \vdots & \vdots & \ddots & \vdots & \vdots & \vdots \\
\vdots & \vdots & \vdots & \ddots & 0 & \vdots & \vdots & \vdots & \vdots & \ddots & \vdots & \vdots & \vdots \\
\vdots & \vdots & \vdots & \ddots & -\frac{\delta}{\mu_X} & 0 & \vdots & \vdots & \vdots & \ddots & \vdots & \vdots & \vdots \\
\vdots & \vdots & \vdots & \ddots & -\frac{\alpha}{\mu_M} & -\frac{\gamma}{\mu_M} & 0 & \vdots & \vdots & \ddots & \vdots & \vdots & \vdots \\
\vdots & \vdots & \vdots & \ddots & \frac{\alpha+\beta+\gamma+\delta}{\mu_X} & -\frac{\beta}{\mu_X} & -\frac{\gamma}{\mu_X} & 0 & \vdots & \ddots & \vdots & \vdots & \vdots \\
\vdots & \vdots & \vdots & \ddots & -\frac{\beta}{\mu_X} & \frac{\alpha+\beta+\gamma+\delta}{\mu_X} & -\frac{\alpha}{\mu_X} & -\frac{\delta}{\mu_X} & 0 & \ddots & \vdots & \vdots & \vdots \\
\vdots & \vdots & \vdots & \ddots & -\frac{\gamma}{\mu_M} & -\frac{\alpha}{\mu_M} & 2\frac{\alpha+\gamma}{\mu_M} & -\frac{\alpha}{\mu_M} & -\frac{\gamma}{\mu_M} & \ddots & \vdots & \vdots & \vdots \\
\vdots & \vdots & \vdots & \ddots & 0 & -\frac{\delta}{\mu_X} & -\frac{\alpha}{\mu_X} & \frac{\alpha+\beta+\gamma+\delta}{\mu_X} & -\frac{\beta}{\mu_X} & \ddots & \vdots & \vdots & \vdots \\
\vdots & \vdots & \vdots & \ddots & \vdots & 0 & -\frac{\gamma}{\mu_X} & -\frac{\beta}{\mu_X} & \frac{\alpha+\beta+\gamma+\delta}{\mu_X} & \ddots & \vdots & \vdots & \vdots \\
\vdots & \vdots & \vdots & \ddots & \vdots & \vdots & 0 & -\frac{\gamma}{\mu_M} & -\frac{\alpha}{\mu_M} & \ddots & \vdots & \vdots & \vdots \\
\vdots & \vdots & \vdots & \ddots & \vdots & \vdots & \vdots & 0 & -\frac{\delta}{\mu_X} & \ddots & \vdots & \vdots & \vdots \\
\vdots & \vdots & \vdots & \ddots & \vdots & \vdots & \vdots & \vdots & 0 & \ddots & \vdots & \vdots & \vdots \\
\vdots & \vdots & \vdots & \ddots & \vdots & \vdots & \vdots & \vdots & \vdots & \ddots & \vdots & \vdots & \vdots \\
\vdots & \vdots & \vdots & \ddots & \vdots & \vdots & \vdots & \vdots & \vdots & \ddots & 0 & \vdots & \vdots \\
\vdots & \vdots & \vdots & \ddots & \vdots & \vdots & \vdots & \vdots & \vdots & \ddots & -\frac{\delta}{\mu_M} & 0 & \vdots \\
\vdots & \vdots & \vdots & \ddots & \vdots & \vdots & \vdots & \vdots & \vdots & \ddots & -\frac{\beta}{\mu_X} & -\frac{\gamma}{\mu_X} & 0 \\
\vdots & \vdots & \vdots & \ddots & \vdots & \vdots & \vdots & \vdots & \vdots & \ddots & \frac{\alpha+\beta+\gamma+\delta}{\mu_X} & -\frac{\alpha}{\mu_X} & -\frac{\delta_e}{\mu_X} \\
\vdots & \vdots & \vdots & \ddots & \vdots & \vdots & \vdots & \vdots & \vdots & \ddots & -\frac{\alpha}{\mu_M} & \frac{\alpha_e+\alpha+\gamma}{\mu_M} & -\frac{\alpha_e}{\mu_M} \\
0 & 0 & 0 & \cdots & 0 & 0 & 0 & 0 & 0 & \cdots & -\frac{\delta_e}{\mu_X} & -\frac{\alpha_e}{\mu_X} & \frac{\alpha_e+\delta_e}{\mu_X}
\end{pmatrix}.$$

To find the normal modes, one has to seek for sinusoidal solutions. For this kind of solutions, Eq. (S1) becomes

$$\mathcal{D}\,\mathcal{U} = \omega^2\,\mathcal{U}. \tag{S2}$$

Therefore, the $3N$ normal modes, with eigenfrequencies ω_k and normal displacements $\mathcal{U}^k$ ($k \in [\![1, 3N]\!]$), are obtained by diagonalizing the dynamical matrix $\mathcal{D}$.

SII. BULK PHONON FREQUENCIES

To obtain the frequencies of the six bulk normal modes, we use the same model as in the previous section SI except that we apply the Born von Karman periodic boundary conditions

to take into account the infinite size of the crystal. In this case, the unit cell of this one-dimensional Bravais lattice contains the three atoms of one layer. For the n^{th} layer, we suppose that the equilibrium positions are na for the Mo atom and $na-d$ and $na+d$ for the two Te atoms. Thus, Mo atoms belonging to adjacent layers are separated by a. With the same notation as in section SI, we seek for solutions in the form of a plane wave with frequency ω and wave vector k : $u_{j,n} = A_j e^{-i(\omega t - kna)}$ where $j = 1, 3$ for Te and $j = 2$ for Mo, and A_j are constants to be determined, whose ratio specify the relative amplitude and phase of vibration of the atoms within each layer. By substituting $u_{j,n}$ into the equations of motion, we obtain three homogeneous equations in terms of A_j. These equations will have a non-zero solution provided that the determinant of the coefficients vanishes. This yields

$$\begin{aligned}\left[\mu_X\omega^2 - (\alpha+\beta+\gamma+\delta)\right]^2 \left[\mu_M\omega^2 - 2(\alpha+\gamma)\right] \\ + (\alpha+\gamma e^{ika})^2(\delta+\beta e^{-ika}) + (\alpha+\gamma e^{-ika})^2(\delta+\beta e^{ika}) \\ - \left[\mu_M\omega^2 - 2(\alpha+\gamma)\right](\delta+\beta e^{ika})(\delta+\beta e^{-ika}) \\ - 2\left[\mu_X\omega^2 - (\alpha+\beta+\gamma+\delta)\right](\alpha+\gamma e^{ika})(\alpha+\gamma e^{-ika}) = 0. \quad \text{(S3)}\end{aligned}$$

The Born von Karman boundary condition leads to N nonequivalent values of k given by $k = \frac{2\pi}{a}\frac{p}{N}$ with p an integer. Eq. (S3) does not need be solved for every k. In fact, for the six bulk normal modes, the displacements of the three atoms within one layer are either in-phase or out-of-phase with the displacements of the atoms of adjacent layers. Therefore, $k = 0$ or $k = \frac{\pi}{a}$ respectively. By Solving Eq. (S3) with $k = 0$ and $k = \frac{\pi}{a}$ and using the symmetry of the atomic displacements, we can get the expression of the six bulk frequencies associated with the low- (LSM, LBM), mid- (iX and oX) and high-frequency (iMX, oMX) modes [1].

$$\omega^-_{\text{low}} = 0, \quad \text{(S4)}$$

$$\omega^+_{\text{low}} = \frac{\alpha+\gamma+2\beta}{2\mu_X} + \frac{\alpha+\gamma}{\mu_M} - \sqrt{\left(\frac{\alpha+\gamma+2\beta}{2\mu_X} - \frac{\alpha+\gamma}{\mu_M}\right)^2 + 2\frac{(\alpha-\gamma)^2}{\mu_X\mu_M}}, \quad \text{(S5)}$$

$$\omega^-_{\text{mid}} = \frac{\alpha+\gamma+2\delta}{\mu_X}, \quad \text{(S6)}$$

$$\omega^+_{\text{mid}} = \frac{\alpha+\gamma+2\delta+2\beta}{\mu_X}, \quad \text{(S7)}$$

$$\omega^-_{\text{high}} = \frac{(2\mu_X+\mu_M)(\alpha+\gamma)}{\mu_X\mu_M}, \quad \text{(S8)}$$

$$\omega^+_{\text{high}} = \frac{\alpha+\gamma+2\beta}{2\mu_X} + \frac{\alpha+\gamma}{\mu_M} + \sqrt{\left(\frac{\alpha+\gamma+2\beta}{2\mu_X} - \frac{\alpha+\gamma}{\mu_M}\right)^2 + 2\frac{(\alpha-\gamma)^2}{\mu_X\mu_M}}. \quad \text{(S9)}$$

From the value of the force constants extracted from the fit of our experimental data (see Table II of the main text), we notice that $|\alpha| \gg |\beta|, |\gamma|, |\delta|$. Thus, we can perform Taylor

developments of Eqs. (S5) and (S9) to get more convenient expressions

$$\omega^{+}_{\text{low}} \approx 4\frac{\beta + 2\gamma}{\mu}, \tag{S10}$$

$$\omega^{+}_{\text{high}} \approx \frac{\alpha\mu^2 + 2\beta\mu_M^2 + \gamma(2\mu_X - \mu_M)^2}{\mu\mu_X\mu_M}, \tag{S11}$$

where $\mu = 2\mu_X + \mu_M$ is the mass per unit area of the unit cell. The relative difference between the results of Eqs. (S10)/(S11) and the exact values obtained using Eqs. (S5)/(S9), respectively, is lower than 1‰.

An interesting quantity than can be deduced from the expressions of the bulk frequencies, for low-, mid- and high-frequency modes, is the bulk Davydov splitting $\Delta\omega = \omega^{+} - \omega^{-}$. Again by performing Taylor expansions, we get the following expressions for the Davydov splitting

$$\Delta\omega_{\text{low}} \approx 2\sqrt{\frac{\beta + 2\gamma}{\mu}}, \tag{S12}$$

$$\Delta\omega_{\text{mid}} \approx \frac{\beta}{\alpha}\left(1 - \frac{\gamma + 2\delta}{2\alpha}\right)\sqrt{\frac{\alpha}{\mu_X}}, \tag{S13}$$

$$\Delta\omega_{\text{high}} \approx \left(\frac{\mu_M^2}{\mu^2}\frac{\beta}{\alpha} - \frac{4\mu_X\mu_M}{\mu^2}\frac{\gamma}{\alpha}\right)\sqrt{\frac{\alpha\mu}{\mu_X\mu_M}}. \tag{S14}$$

The deviation of the results of Eqs. (S12) and (S13) from the exact values deduced from Eqs. (S4)-(S7) is lower than 1%, and the deviation of the results of Eqs. (S14) from the exact values deduced from Eqs. (S8) and (S9) is lower than 10%.

Interestingly, the high-frequency Davydov splitting (Eq. (S14)) is the only one that can be negative since $\alpha \gg \beta, \gamma, \delta$. If $\frac{\mu_M}{4\mu_X}\frac{\beta}{\gamma} \geq 1$ the splitting is normal and the bulk high-frequency in-phase mode has a lower frequency than the bulk high-frequency out of phase mode. Otherwise, the splitting is anomalous, as it has been reported for the iMX mode in bulk transition metal dichalcogenides [6].

SIII. NORMAL MODE DISPLACEMENTS

Figures S2 to S7 show the normal mode displacements associated with the LSM, iX, iMX, LBM, oX, and oMX modes in N-layer $MoTe_2$.

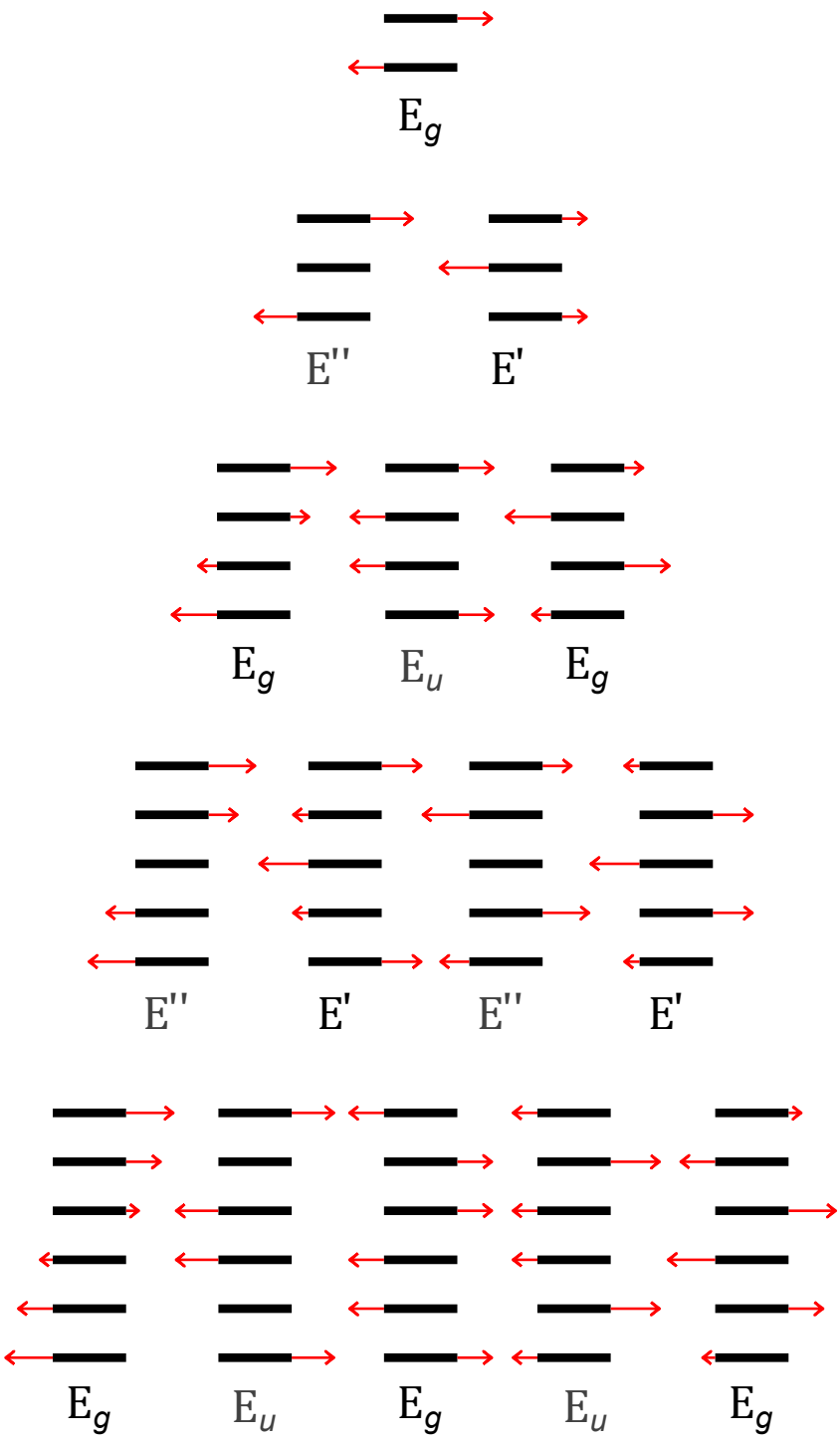

FIG. S2: Calculated normal displacements associated with the LSM in $N = 1$ to $N = 6$ layers $MoTe_2$. The size of the arrows is proportional to the amplitude of $u^k_{i,j}$ of the normal displacement obtained from the solution of Eq. (S1). The frequencies of the modes increase from left to right. The irreductible representation of each normal mode is indicated. The modes that are Raman-active in our geometry appear in black. The other modes appear in grey.

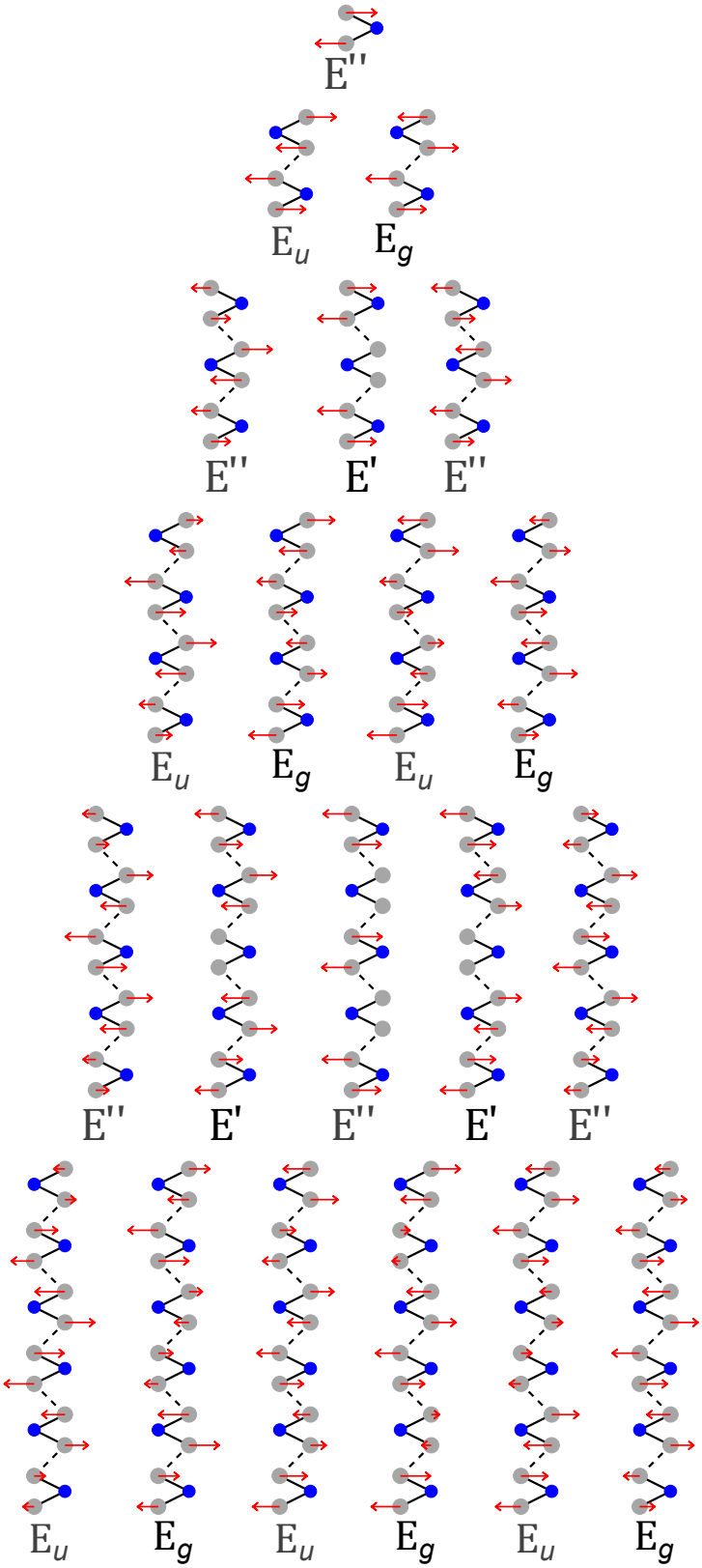

FIG. S3: Same as Fig. S2 for the iX modes in $N = 1$ to $N = 6$ layers $MoTe_2$.

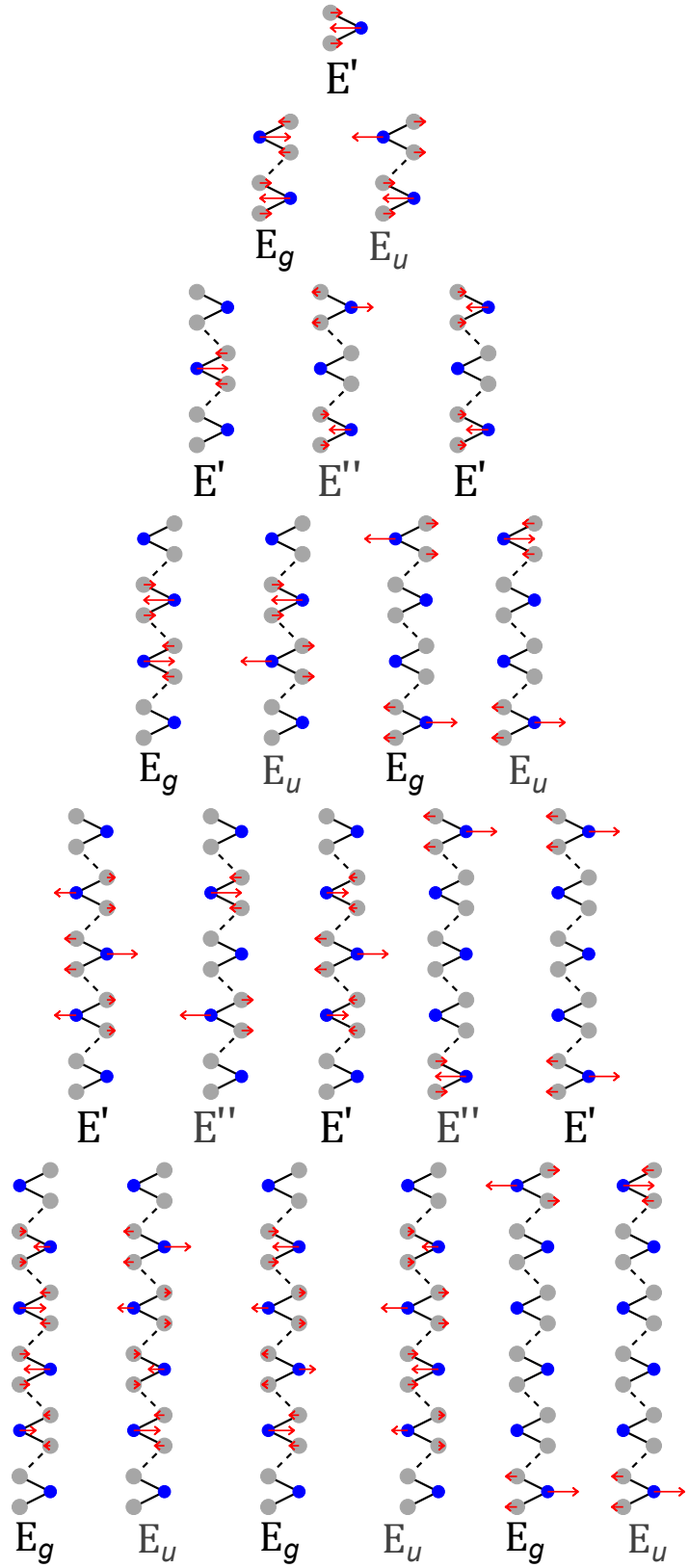

FIG. S4: Same as Fig. S2 for the iMX modes in $N = 1$ to $N = 6$ layers $MoTe_2$.

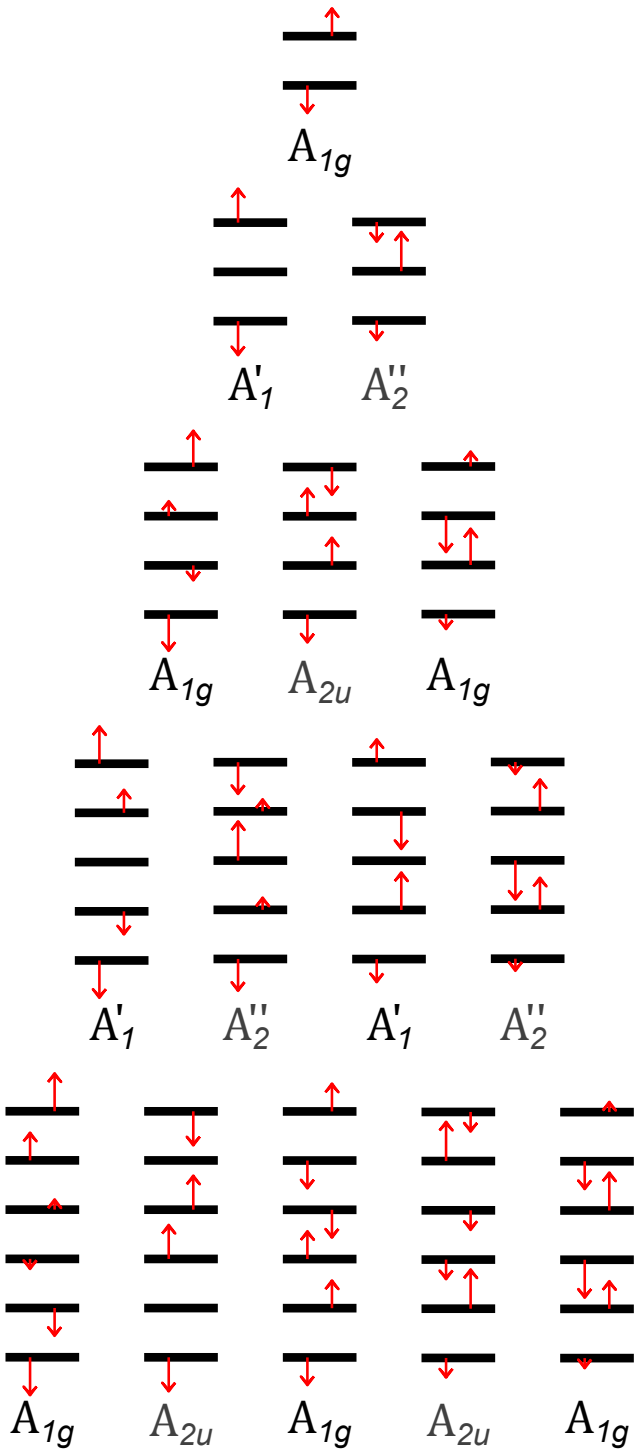

FIG. S5: Same as Fig. S2 for the LBM in $N = 1$ to $N = 6$ layers $MoTe_2$.

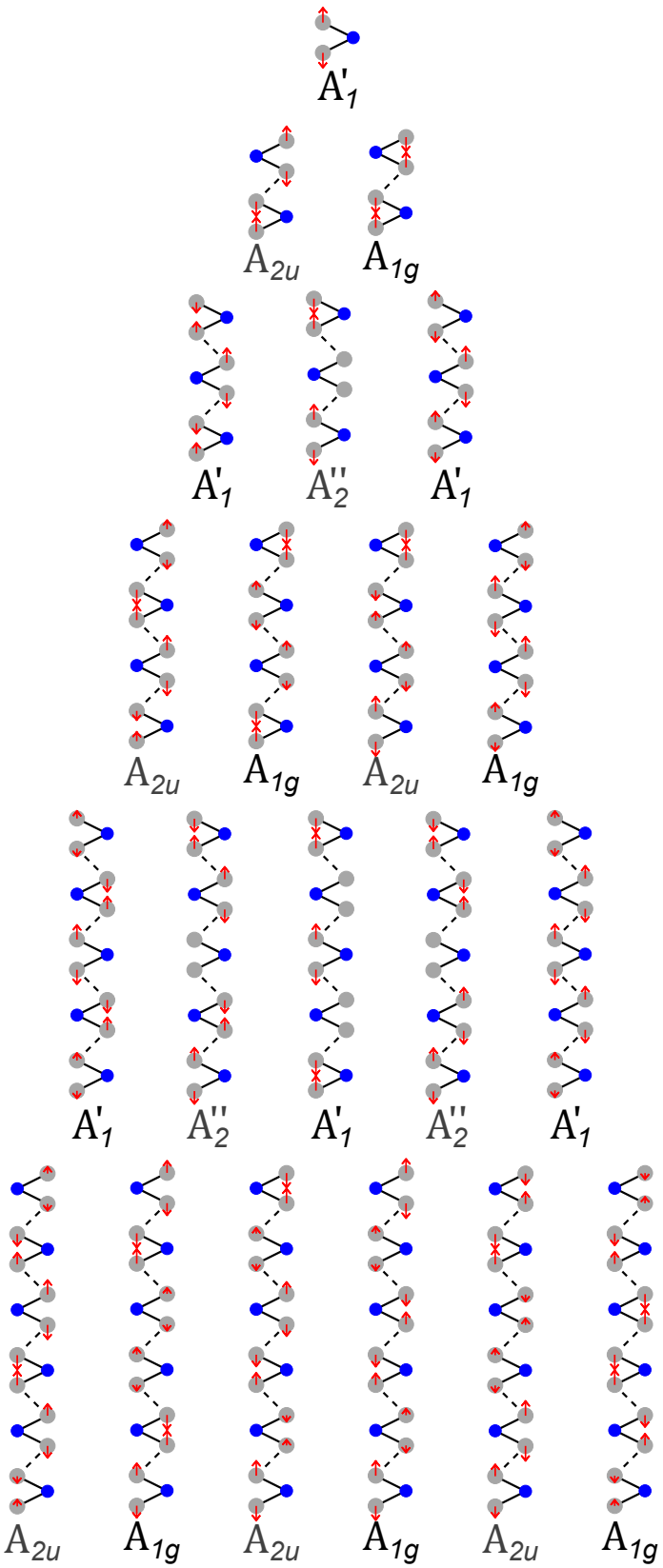

FIG. S6: Same as Fig. S2 for the oX modes in $N = 1$ to $N = 6$ layers $MoTe_2$.

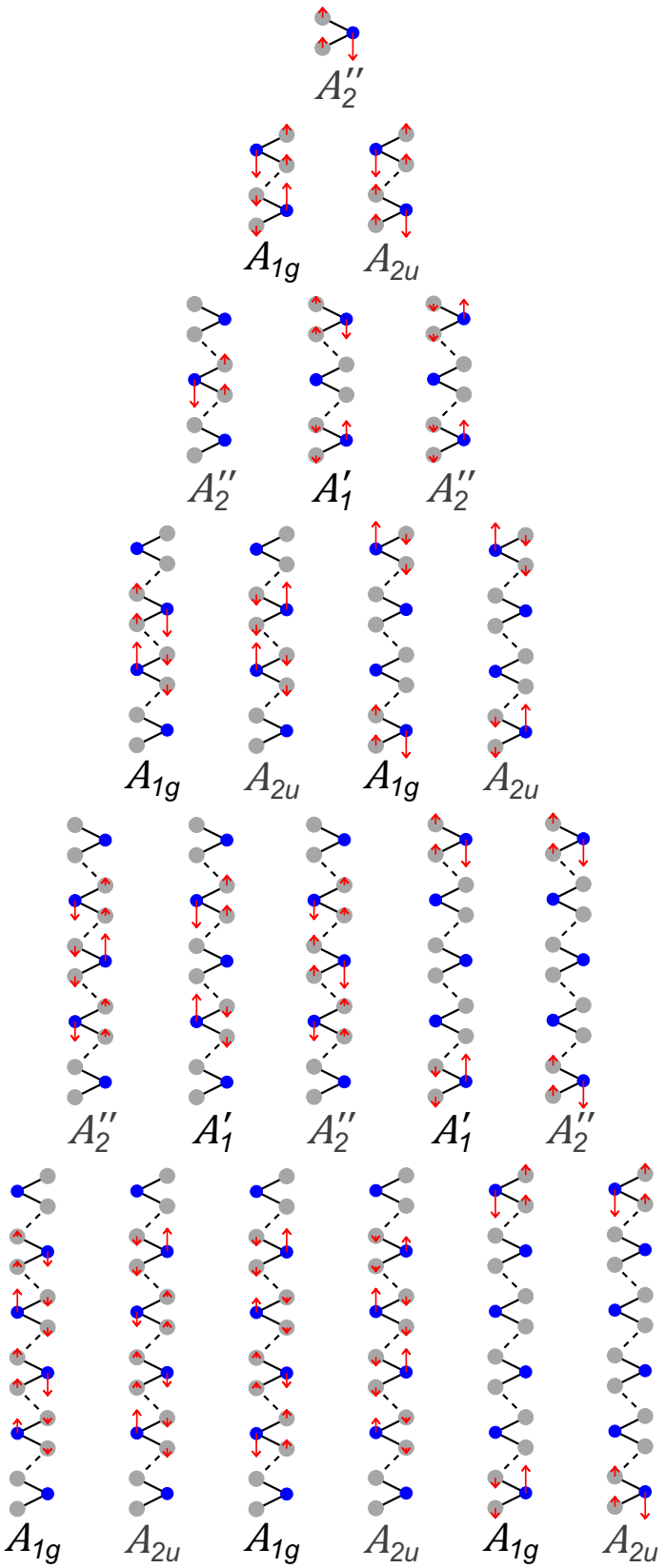

FIG. S7: Same as Fig. S2 for the oMX modes in $N = 1$ to $N = 6$ layers $MoTe_2$.

SIV. THE EMPIRICAL BOND POLARIZABILITY MODEL

In the Placzek approximation, the Raman intensity for non resonant first order scattering is given by

$$I^{\nu} \propto |\mathbf{e}_i \cdot \mathbf{A}^{\nu} \cdot \mathbf{e}_s|^2 \frac{1}{\omega_\nu}(n_\nu + 1), \tag{S15}$$

where $\mathbf{e}_i$ and $\mathbf{e}_s$ are the polarizations of the incident and the scattered light respectively, ω_ν is the Raman frequency, and $n_\nu = [\exp(\hbar\omega_\nu/k_B T) - 1]^{-1}$ with T being the temperature. The Raman tensor $\mathbf{A}^{\nu}$ is related to the change of the polarizability α under atomic displacement. It can be calculated as

$$A^{\nu}_{ij} = \sum_{k\gamma} B^{k\gamma}_{ij} \frac{\xi^{\nu}_{k\gamma}}{\sqrt{M_\gamma}} \tag{S16}$$

where $\xi^{\nu}_{k\gamma}$ is the k^{th} Cartesian component of atom γ of the ν^{th} orthonormal vibrational eigenvector M_γ is the atomic mass, and

$$B^{k\gamma}_{ij} = \frac{\partial^3 \mathcal{E}}{\partial E_i \partial E_j \partial u_{k\gamma}} = \frac{\partial \alpha_{ij}}{\partial u_{k\gamma}}. \tag{S17}$$

$\mathcal{E}$ is the total energy in the unit cell, E is a uniform electric field, $u_{k\gamma}$ is the k^{th} component of the atomic displacement $\boldsymbol{u}$ of the atom γ and α_{ij} is the electronic polarizability tensor. The bond polarizability model approximates the total polarizability of the atom as the sum of the individual bond polarizabilities. Under the assumption that the bonds have cylindrical symmetry, the polarizability tensor for a single bond can be written as

$$\begin{aligned} \alpha^{b}_{ij} &= \frac{1}{3}(2\alpha_p + \alpha_l)\delta_{ij} + (\alpha_l - \alpha_p)\left(\hat{R}_i \hat{R}_j - \frac{1}{3}\delta_{ij}\right) \\ &= \alpha_p \delta_{ij} + (\alpha_l - \alpha_p)\hat{R}_i \hat{R}_j \end{aligned} \tag{S18}$$

where α_l and α_p are longitudinal and perpendicular polarizabilities of the bond and $\hat{R}_i$ are the components of the unit vector along the bond. Moreover, in the model, the polarizabilities depend only on the length of the bond ($R = \sqrt{\boldsymbol{R} \cdot \boldsymbol{R}}$). The bond vector $\boldsymbol{R}$ joining atoms γ to atom γ' is given by

$$\boldsymbol{R} = \boldsymbol{R}_\gamma - \boldsymbol{R}_{\gamma'} + \boldsymbol{u}_\gamma - \boldsymbol{u}_{\gamma'} \tag{S19}$$

and

$$\begin{aligned} \frac{\partial \alpha(R)}{\partial u_{k\gamma}} &= \frac{\partial \alpha(R)}{\partial R}\frac{\partial R}{\partial u_{k\gamma}} \\ &= \frac{\partial \alpha(R)}{\partial R}\frac{1}{2\sqrt{\mathbf{R}\cdot\mathbf{R}}}\left(\mathbf{R}\cdot\frac{\partial \mathbf{R}}{\partial u_{k\gamma}} + \frac{\partial \mathbf{R}}{\partial u_{k\gamma}}\cdot\mathbf{R}\right) \\ &= \frac{\partial \alpha(R)}{\partial R}\frac{1}{2R}(-2R_k) \end{aligned} \tag{S20}$$

Hence,

$$\frac{\partial \alpha(R)}{\partial u_{k\gamma}(l)} = \alpha' \hat{R}_k \tag{S21}$$

where $\alpha' = -\frac{\partial \alpha(R)}{\partial R}$. The contribution of a particular bond b to the B tensor is therefore

$$\frac{\partial \alpha^b_{ij}}{\partial u_{k\gamma}} = \alpha'_p \hat{R}_k \delta_{ij} + (\alpha'_l - \alpha'_p)\hat{R}_i \hat{R}_j \hat{R}_k + (\alpha_l - \alpha_p)((\partial_k \hat{R}_i)\hat{R}_j + (\partial_k \hat{R}_j)\hat{R}_i) \tag{S22}$$

with

$$\partial_k \hat{R}_i = -\frac{1}{R}\left(\delta_{ik} - \hat{R}_i \hat{R}_k\right) \tag{S23}$$

In the $2H$ structure of $MoTe_2$, the Molybdenum atom is bonded to six Tellurium atoms and the Tellurium atom is bonded to three Molybdenum atoms. In our calculations, we neglect the weak inter-layer bonds. That is the reason why we don't get a finite peak for the E^2_{2g} (shear) mode with this model.

The calculated B tensors are as follows:

$$B_x(\mathrm{Te}_1) = \begin{pmatrix} 0 & \frac{-p}{2} & q \\ \frac{-p}{2} & 0 & 0 \\ q & 0 & 0 \end{pmatrix} \qquad B_y(\mathrm{Te}_1) = \begin{pmatrix} \frac{-p}{2} & 0 & 0 \\ 0 & \frac{p}{2} & q \\ 0 & q & 0 \end{pmatrix} \qquad B_z(\mathrm{Te}_1) = \begin{pmatrix} a & 0 & 0 \\ 0 & a & 0 \\ 0 & 0 & b \end{pmatrix}$$

$$B_x(\mathrm{Mo}_1) = \begin{pmatrix} 0 & p & 0 \\ p & 0 & 0 \\ 0 & 0 & 0 \end{pmatrix} \qquad B_y(\mathrm{Mo}_1) = \begin{pmatrix} p & 0 & 0 \\ 0 & -p & 0 \\ 0 & 0 & 0 \end{pmatrix} \qquad B_z(\mathrm{Mo}_1) = \begin{pmatrix} 0 & 0 & 0 \\ 0 & 0 & 0 \\ 0 & 0 & 0 \end{pmatrix}$$

$$B_x(\mathrm{Te}_2) = \begin{pmatrix} 0 & \frac{-p}{2} & -q \\ \frac{-p}{2} & 0 & 0 \\ -q & 0 & 0 \end{pmatrix} \quad B_y(\mathrm{Te}_2) = \begin{pmatrix} \frac{-p}{2} & 0 & 0 \\ 0 & \frac{p}{2} & -q \\ 0 & -q & 0 \end{pmatrix} \quad B_z(\mathrm{Te}_2) = \begin{pmatrix} -a & 0 & 0 \\ 0 & -a & 0 \\ 0 & 0 & -b \end{pmatrix}$$

$$B_x(\mathrm{Te}_3) = \begin{pmatrix} 0 & \frac{p}{2} & q \\ \frac{p}{2} & 0 & 0 \\ q & 0 & 0 \end{pmatrix} \qquad B_y(\mathrm{Te}_3) = \begin{pmatrix} \frac{p}{2} & 0 & 0 \\ 0 & \frac{-p}{2} & q \\ 0 & q & 0 \end{pmatrix} \qquad B_z(\mathrm{Te}_3) = \begin{pmatrix} a & 0 & 0 \\ 0 & a & 0 \\ 0 & 0 & b \end{pmatrix}$$

$$B_x(\mathrm{Mo}_2) = \begin{pmatrix} 0 & -p & 0 \\ -p & 0 & 0 \\ 0 & 0 & 0 \end{pmatrix} \quad B_y(\mathrm{Mo}_2) = \begin{pmatrix} -p & 0 & 0 \\ 0 & p & 0 \\ 0 & 0 & 0 \end{pmatrix} \qquad B_z(\mathrm{Mo}_2) = \begin{pmatrix} 0 & 0 & 0 \\ 0 & 0 & 0 \\ 0 & 0 & 0 \end{pmatrix}$$

$$B_x(\mathrm{Te}_4) = \begin{pmatrix} 0 & \frac{p}{2} & -q \\ \frac{p}{2} & 0 & 0 \\ -q & 0 & 0 \end{pmatrix} \quad B_y(\mathrm{Te}_4) = \begin{pmatrix} \frac{p}{2} & 0 & 0 \\ 0 & \frac{-p}{2} & -q \\ 0 & -q & 0 \end{pmatrix} \quad B_z(\mathrm{Te}_4) = \begin{pmatrix} -a & 0 & 0 \\ 0 & -a & 0 \\ 0 & 0 & -b \end{pmatrix}$$

The values of the constants a, b, p and q, in terms of the polarizabilities and their derivatives, obtained after substituting the $MoTe_2$ lattice parameters are:

$$\begin{aligned} a &= -0.24\alpha_l - 0.56\alpha_l' + 0.24\alpha_t - 1.40\alpha_t' \\ b &= 0.48\alpha_l - 0.84\alpha_l' - 0.48\alpha_t - 1.12\alpha_t' \\ p &= 0.28\alpha_l + 0.64\alpha_l' - 0.28\alpha_t - 0.64\alpha_t' \\ q &= 0.18\alpha_l - 0.56\alpha_l' - 0.18\alpha_t + 0.56\alpha_t' \end{aligned} \tag{S24}$$

SV. RAMAN SPECTRA FROM THE BOND POLARIZABILITY MODEL

With the bond polarizability model, we can assign a Raman intensity to each Raman frequency obtained with the force constant model. While active Raman modes agree with group theory and experimental data, the model does not include Raman resonance effects, and some discrepancies arise when we compare with experimental spectra. Figure S8 shows the theoretical Raman spectra for the modes iX, oX, iMX, and oMX. The spectra for different n values are offset for clarity. The iX mode has $\lfloor N/2 \rfloor$ active subfeatures in $N-$layer $MoTe_2$ and is in nice agreement with the spectra of Fig. 3.

For the iMX mode, there are two close peaks for $N \geq 3$; one being an inner mode (with lower frequency) and the other being a surface mode (with higher frequency). The difference in their frequencies is around 0.5 cm^{-1}.The absolute intensity of the inner mode increases almost linearly with number of layers, as there are more layers vibrating, whereas the absolute intensity of the surface mode is independent of number of layers, as only the outer molecules are vibrating. As a result, the relative intensity of the surface mode drops as N increases, and thus the maximum of the combined peak shifts to smaller frequencies as N increases.

In the case of the oX mode our model reproduces the $\lceil N/2 \rceil$ active subfeatures well, but it fails in describing the observed relative intensity between peaks. The highest frequency peak in the oX-mode feature has much larger relative intensity than the rest of the peaks in the model, which is in contrast to our measurements, where all the phonons have comparable intensities. We can understand this result from the shape of the B_z tensors shown above. The largest contribution occurs when all the Te layers are out-of-phase with the neighboring Te layers. In case two layers vibrate in-phase, they cancel each other, and therefore increasing the number of layers in-phase reduces the intensity drastically. The similar intensity of the A_1' peaks suggest the participation of Raman resonance effects.

For the oMX mode, the surface phonons, which are split from the inner modes, have much larger intensity than the inner modes in the model. From the Raman tensors, if tellurium atoms in the same layer vibrate in-phase and with identical amplitude, the intensity is identically zero. Only differences in the amplitudes can generate Raman signal, which will be very

small in comparison with the intensity of the oX modes. The largest amplitude differences are due to surface phonons, which carry most of the contribution to the Raman intensity and it results in the sole peak observed in the Raman spectra. A feature assigned to the inner modes is slightly visible in the measured spectra at $E_L = 1.96$ eV (see Fig. 3(c) in the main text) but not at $E_L = 2.33$ eV, which, again, suggests a resonance effect at $E_L = 1.96$ eV, similar to the oX mode.

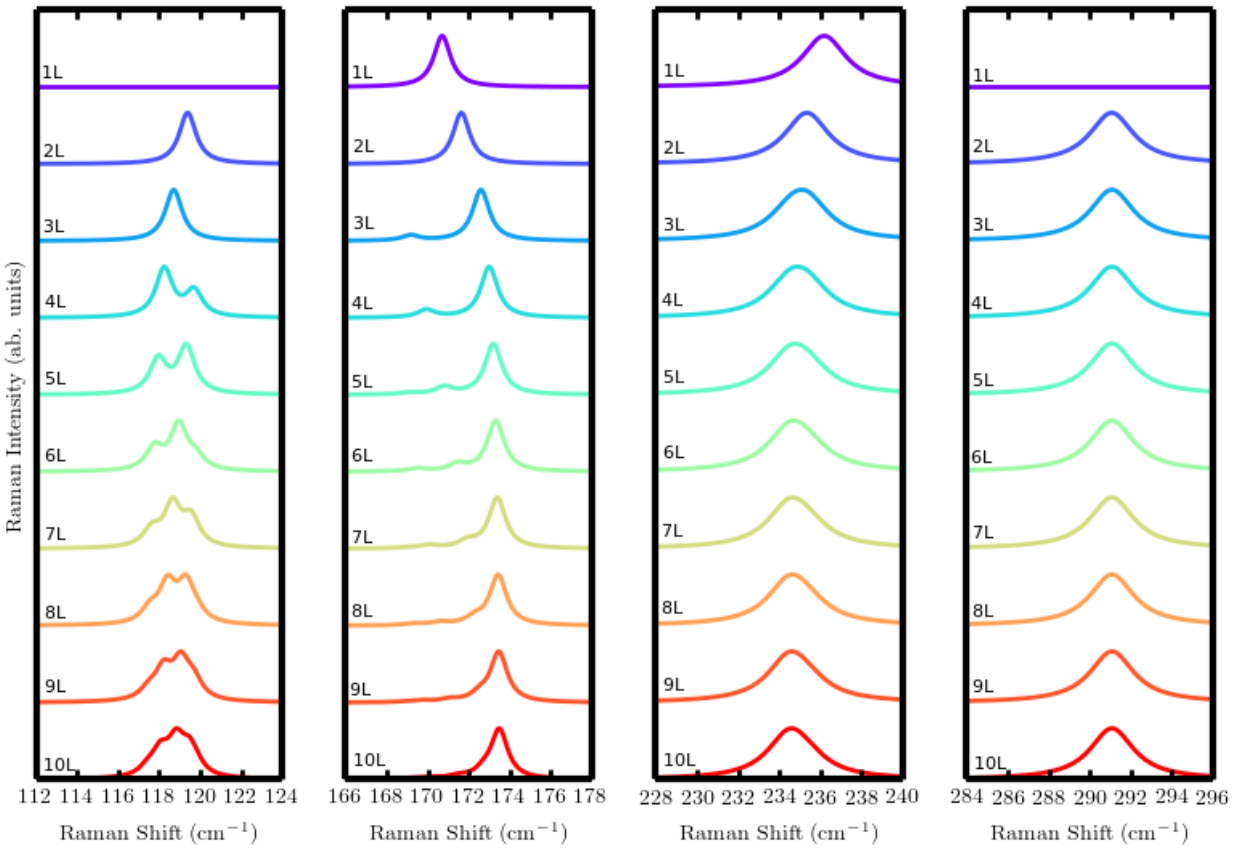

(a) iX Model (b) oX Mode (c) iMX Mode (d) oMX Mode

FIG. S8: Raman Spectra obtained with the bond polarizability model.

SVI. AB-INITIO BULK PHONON MODES

We have complemented the empirical model with *ab-initio* calculations of the phonon modes for bulk $MoTe_2$. We have used density functional perturbation theory (DFPT) [7] as implemented in the Quantum Espresso code [8]. We used the local-density approximation (LDA) which does not properly take into account van der Waals interaction between the layers but nevertheless gives decent result for the phonons of many layered systems because it overestimates the weak covalent part of the inter-layer bonding. The energy cutoff is 80 Ry, and the Monkhorst-Pack sampling of the $\mathbf{k}-$grid is $12\times12\times4$. The optimized lattice vectors are $a = 3.499$ Åand $c = 13.829$ Å. Figure S9 shows the ab-initio frequencies together with the corresponging phonon eigenvectors. We have grouped the phonon modes in Davydov pairs, except the shear and layer-breathing modes (whose "Davydov partner" would be a zero frequency acoustic mode). We observe a positive Davydov splitting for the iX, oX and oMX modes and a negative Davydov splitting for the mode iMX mode, as reported for other transition metal dichalcogenides [6]. The calculated Davydov-splitting of the iX mode is 2.1 cm^{-1} (compared to the 2.7 cm^{-1} extrapolated from the measurements). For the oX mode, we obtain a splitting of 3.2 cm^{-1} (compared to 4.7 cm^{-1} from the experiments). The agreement between calculations and experiment is not perfect because of the lack of a proper treatment of van der Waals interaction with local exchange-correlation functionals. The predicted Davydov-Splitting for the oMX mode is 5.8 cm^{-1}. For the calculation of the frequency of the A_{2u} mode, we have not taken into account the coupling to an external-electric field (Lydanne-Sachs-Teller interaction) that would lead to an up-shift of this mode. However, in layers of finite width, this interaction is absent.

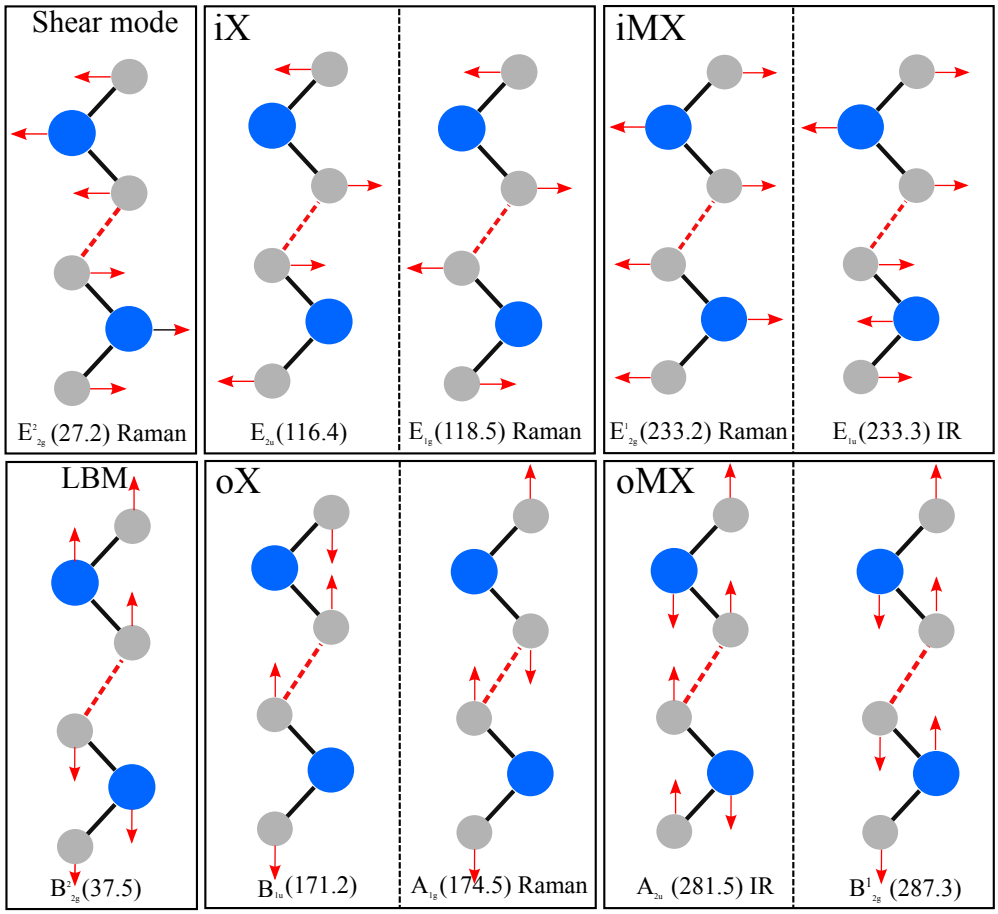

FIG. S9: Optical phonon modes of bulk $MoTe_2$. In the first row, modes with in-plane polarization in ascending order of frequency. In the second row, the out-of-plane modes are shown. Davydov pairs of phonon modes are plotted in one box.

SVII. ADDITIONAL RAMAN MEASUREMENTS

Figure S10 shows the raw Raman spectra of N-layer $MoTe_2$ recorded at $E_L = 2.33$ eV and $E_L = 1.96$ eV. Note that the iX mode has not been studied at $E_L = 1.96$ eV due to the relatively large bandwidth of our Notch filter at $E_L = 1.96$ eV.

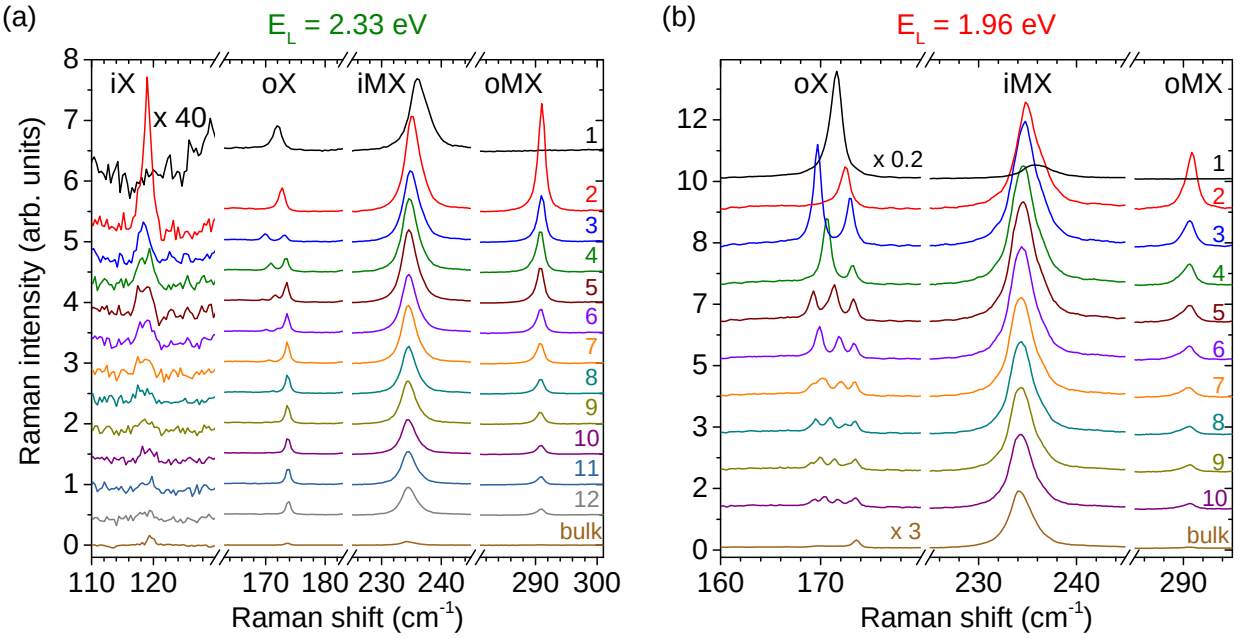

FIG. S10: Micro-Raman spectra of $N-$layer $MoTe_2$ recorded under the same conditions at a photon energy of (a) 2.33 eV and (b) 1.96 eV. The spectra are vertically offset for clarity.

Figure S11 shows Raman spectra of the oX, iMX and oMX modes in N-layer $MoTe_2$ recorded at $E_L = 2.33$ eV. The results recorded at $E_L = 1.96$ eV are discussed in the main manuscript. At $E_L = 2.33$ eV, the Davydov splitting also appears clearly for the oX feature, although the highest energy subfeature contains most of the oscillator strength for $N \geq 6$. The iMX feature also downshifts as N increases and no appreciable splitting can be resolved. However, in contrast with our results at $E_L = 1.96$ eV, the oMX feature does not exhibit any measurable splitting at $E_L = 2.33$ eV.

The corresponding fan diagrams associated with oX-, iMX and oMX-mode frequencies recorded at $E_L = 2.33$ eV are shown in Fig. S12, together with the fan diagrams for oX and oMX modes extracted from the data recorded at $E_L = 1.96$ eV and discussed in details in the main text. These two sets of data are very consistent with each other. Still, we can notice a small rigid shift of approximately 0.2 cm^{-1} which is smaller than the resolution of our experimental setup. This shift presumably arises from uncertainties (below our spectral resolution) in the calibration of our spectrometer. Importantly such a small shift has a negligible influence on the determination of the force constants. Indeed, the latter vary by

less 1.5 % if one uses the oX, oMX and iMX frequencies recorded at $E_{\mathrm{L}} = 2.33$ eV instead of their values recorded at $E_{\mathrm{L}} = 1.96$ eV in the global fitting procedure described in the main manuscript.

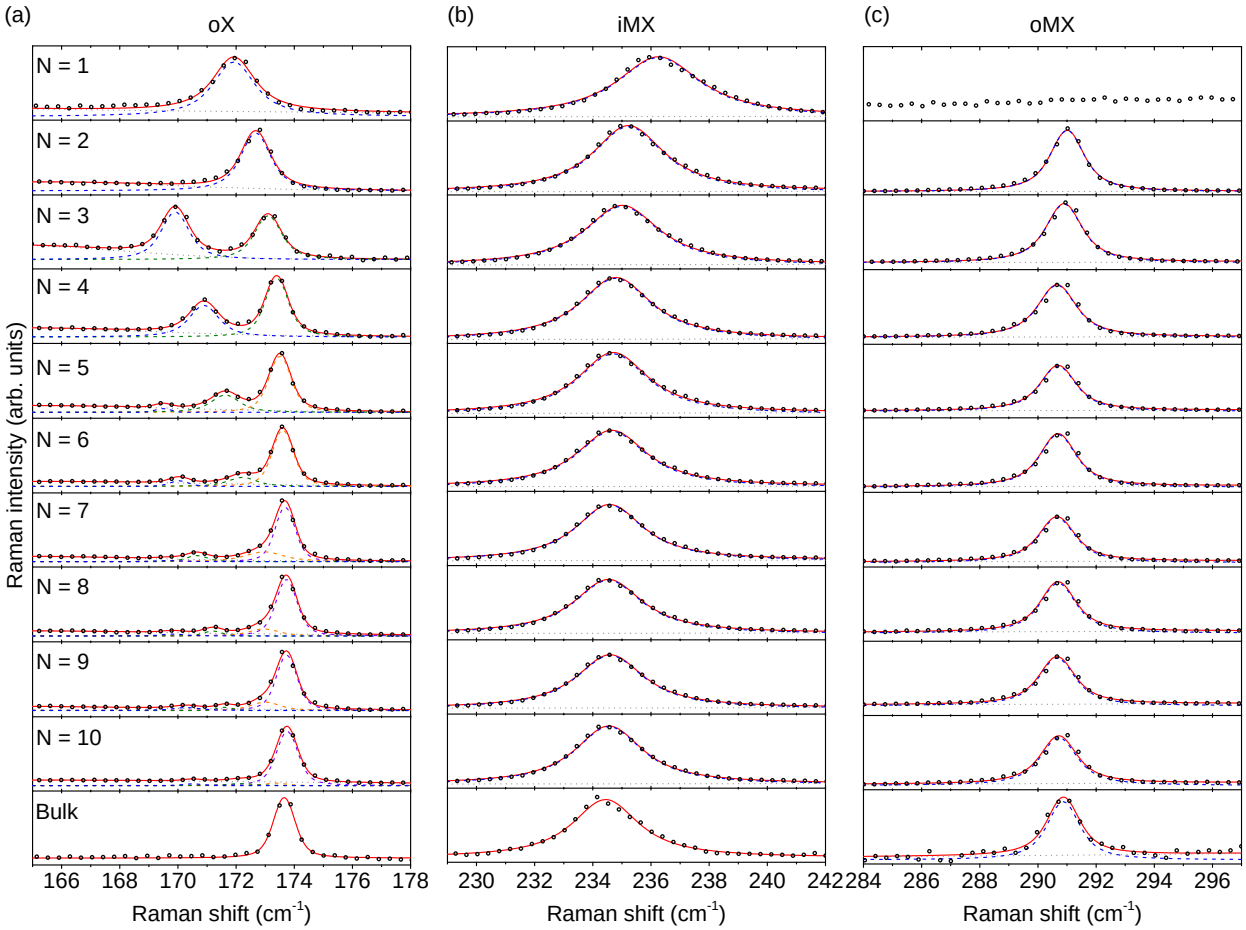

FIG. S11: Normalized Micro-Raman spectra of the (a) oX, (b) iMX, and (c) oMX mode-features in $N-$layer $MoTe_2$ recorded at $E_{\mathrm{L}} = 2.33$ eV. The measured Raman features (symbols) are fit to Voigt profiles (solid lines). For the modes that show a Davydov splitting, each subpeak is represented with a colored dashed line. A featureless background (grey dashed line) has been considered when necessary.

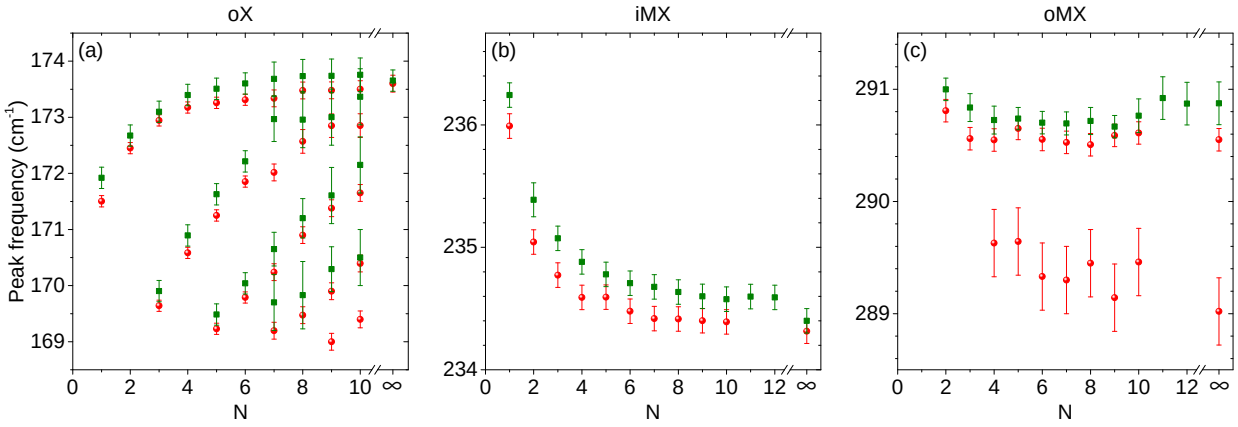

FIG. S12: Frequencies of the (a) oX, (b) iMX and (c) oMX modes extracted from Voigt fits as a function of the number of layers N. Green squares (red circles) correspond to data recorded at $E_{\mathrm{L}} = 2.33$ eV ($E_{\mathrm{L}} = 1.96$ eV).

[1] Xin Luo, Yanyuan Zhao, Jun Zhang, Qihua Xiong, and Su Ying Quek, "Anomalous frequency trends in mos_2 thin films attributed to surface effects," Phys. Rev. B **88**, 075320 (2013).

[2] Changgu Lee, Hugen Yan, Louis E. Brus, Tony F. Heinz, James Hone, and Sunmin Ryu, "Anomalous Lattice Vibrations of Single- and Few-Layer MoS_2," ACS Nano **4**, 2695–2700 (2010).

[3] Mahito Yamamoto, Sheng Tsung Wang, Meiyan Ni, Yen-Fu Lin, Song-Lin Li, Shinya Aikawa, Wen-Bin Jian, Keiji Ueno, Katsunori Wakabayashi, and Kazuhito Tsukagoshi, "Strong Enhancement of Raman Scattering from a Bulk-Inactive Vibrational Mode in Few-Layer $MoTe_2$," ACS Nano **8**, 3895–3903 (2014).

[4] Xin Luo, Yanyuan Zhao, Jun Zhang, Minglin Toh, Christian Kloc, Qihua Xiong, and Su Ying Quek, "Effects of lower symmetry and dimensionality on raman spectra in two-dimensional wse_2," Phys. Rev. B **88**, 195313 (2013).

[5] Yanyuan Zhao, Xin Luo, Hai Li, Jun Zhang, Paulo T. Araujo, Chee Kwan Gan, Jumiati Wu, Hua Zhang, Su Ying Quek, Mildred S. Dresselhaus, and Qihua Xiong, "Interlayer Breathing and Shear Modes in Few-Trilayer MoS_2 and WSe_2," Nano Letters **13**, 1007–1015 (2013).

[6] T. J. Wieting, A. Grisel, and F. Lvy, "Interlayer bonding and localized charge in $MoSe_2$ and α-$MoTe_2$," Physica B+C **99**, 337–342 (1980).

[7] Stefano Baroni, Stefano de Gironcoli, Andrea Dal Corso, and Paolo Giannozzi, "Phonons and related crystal properties from density-functional perturbation theory," Rev. Mod. Phys. **73**, 515–562 (2001).

[8] Paolo Giannozzi, Stefano Baroni, Nicola Bonini, Matteo Calandra, Roberto Car, Carlo Cavazzoni, Davide Ceresoli, Guido L Chiarotti, Matteo Cococcioni, Ismaila Dabo, Andrea Dal Corso, Stefano de Gironcoli, Stefano Fabris, Guido Fratesi, Ralph Gebauer, Uwe Gerstmann, Christos Gougoussis, Anton Kokalj, Michele Lazzeri, Layla Martin-Samos, Nicola Marzari, Francesco Mauri, Riccardo Mazzarello, Stefano Paolini, Alfredo Pasquarello, Lorenzo Paulatto, Carlo Sbraccia, Sandro Scandolo, Gabriele Sclauzero, Ari P Seitsonen, Alexander Smogunov, Paolo Umari, and Renata M Wentzcovitch, "Quantum espresso: a modular and open-source software project for quantum simulations of materials," Journal of Physics: Condensed Matter **21**, 395502 (2009).